



The effect of nitrogen implantation on resistive switching of tetrahedral amorphous carbon films

V.K. Nagareddy^a, A.K. Ott^b, C. Dou^b, T. Tsvetkova^c, M. Sandulov^c, M.F. Craciun^a, A.C. Ferrari^b, C.D. Wright^{a,*}

^a Centre for Graphene Science, College of Engineering, Mathematics and Physical Sciences, University of Exeter, Exeter EX4 4QF, UK

^b Cambridge Graphene Centre, University of Cambridge, Cambridge CB3 0FA, UK

^c Institute of Solid State Physics, Bulgarian Academy of Sciences, 1784 Sofia, Bulgaria

ABSTRACT

We report the effect of nitrogen implantation on the resistance switching of tetrahedral amorphous carbon (ta-C) films. Both unimplanted and implanted films show resistive switching, with a characteristic threshold voltage required to switch the films from the high-resistance to the low-resistance state. The switching voltages for the unimplanted films are between 7 and 10 V for ta-C films of thickness 15 to 40 nm. These are significantly reduced upon implantation by up to 60% when using an implantation dose $\sim 3 \times 10^{15} \text{ cm}^{-2}$. We attribute this to increased sp^2 bonding and clustering in the implanted films. This demonstrates the importance of sp^2 clustering for resistive-switching in sp^3 -rich ta-C films.

1. Introduction

Non-volatile resistive-switching (RS) memories are promising alternatives to traditional Si-based memories, such as dynamic resistive random access memory (DRAM) and Flash, since they potentially offer scalability to nanometre dimensions [1,2], along with fast ($< 10 \text{ ns}$) [3], low-power switching (pJ range) [3], as well as a simple two-terminal device configuration [1–3]. The basic operating scheme of RS-based devices is as follows [3]: for binary memory applications, the active material is electrically switched between a high-resistance (HRS or RESET) and a low-resistance (LRS or SET) state by the application of a voltage; readout is carried out at a voltage well below that required for switching. Advanced functionalities, such as multi-state memory [4,5], logic [4], arithmetic [6] and neuromorphic (brain-like) processing (where processes can be handled in parallel) can also be obtained by exploiting intermediate resistive states and a ‘plasticity’ (whereby the material adapts to changes) inherent in many RS materials [3–6].

RS has been observed in several different material types [1–3,7], such as transition-metal-oxides (TMOs) [8], e.g. TiO_2 [9], SrTiO_3 [10], Cu_2O [11], NiO [12], TaO_x [13], VO_2 [14], HfO_2 [15] etc., perovskite-oxides, e.g. PrCaMnO_3 [16], SrTiO_3Cr [17], chalcogenide phase-change alloys such as $\text{Ge}_2\text{Sb}_2\text{Te}_5$ [6,7,18] and various layered materials (see e.g. Refs. [3,19–21]). RS has also been demonstrated in amorphous carbon films, both sp^2 -rich [1,22], where write-once operation is usually observed [1,22], and sp^3 -rich, such as tetrahedral amorphous carbon (ta-C), where reversible switching was

reported [23–32]. Carbon-based memories potentially offer significant advantages over other RS materials. They are fast, with few-ns switching times [23,27,28]. They are also monoatomic and scalable to small cell sizes in the sub-100 nm range (see e.g. Ref. [28]). They also offer good temperature stability, with data retention well above room temperature (e.g. at 300°C for 600 min in Ref. [24]), making them also suitable for applications in ‘harsh’ environments, where the material would be exposed to high temperatures, such as in the automotive [32] and aerospace sectors [32]. Furthermore, they are environmentally sustainable, since carbon is non-toxic [33] and expected to have easy end-of-use disposal/recycling [33].

Reversible RS in ta-C films was reported by a number of researchers: e.g., Ref. [23] demonstrated RS in a W/ta-C/W structure, with short ($\sim 10 \text{ ns}$) SET and very short ($\sim 1 \text{ ns}$) RESET pulses, a high resistance ratio (> 1000) and good read-endurance (over 10^{13} read cycles at 75°C). Refs. [24, 26] reported write endurance, i.e. the number of times the memory can be switched between states before one of the states becomes irreversible, of > 1000 , along with studies of scalability down to cell sizes $\sim 100 \text{ nm}$ in W/ta-C/Pt devices.

A number of mechanisms have been suggested to explain RS in amorphous carbons, including sp^2 filamentation [23,24,26,28,31,34], sp^2 clustering [22], metal filamentation due to migration of electrode materials [25,29] and electron trapping/de-trapping from defects [30]. Density functional theory and molecular dynamics simulations of confined cell ta-C devices indicate that the switching process is thermally driven via Joule heating. During SET, a small proportion ($\sim 2\text{--}3\%$) of sp^3 bonded atoms in

* Corresponding author.

E-mail address: david.wright@exeter.ac.uk (C.D. Wright).

Table 1
Implantation parameters.

Film thickness (nm)	Ion energy (keV)	Depth of penetration R_p (nm)	Straggle ΔR_p (nm)
40	20	28	8
15	6	15	7

the hottest part of the device re-hybridize to sp^2 , leading to the formation of a conductive filament (CF) via connected sp^2 clusters. On RESET, a few hundred sp^2 bonded atoms (amongst the few thousands in the CF conductive pathway) re-hybridize to sp^3 , causing CF fragmentation [28].

If such sp^2 filamentation and/or clustering is responsible for RS, then N_2 implantation might affect the RS properties, since N_2 incorporation into ta-C can enhance sp^2 bonding (see e.g. Refs. [35–38]). Thus, we here study the effects of N_2 implantation on RS of ta-C films deposited by filtered cathodic vacuum arc (FCVA) [39], with thicknesses ranging from 15 to 40 nm, implanted at ion doses ranging from 1×10^{13} to $3 \times 10^{15} \text{ cm}^{-2}$. X-ray photoelectron spectroscopy (XPS) and multi-wavelength Raman spectroscopy are used to analyse the influence of the N_2 implantation on chemical composition and structural characteristics. Conductive atomic force microscopy (CAFM) is used to probe the RS characteristics. We find that implantation helps facilitate the SET process, reducing the characteristic threshold voltage required to switch the devices. We attribute this to the effect of nitrogen implantation on the number and distribution of sp^2 clusters in the implanted films, demonstrating their importance for RS in sp^3 -rich ta-C films.

2. Experimental

Ta-C memory structures are prepared as follows. First, Pt (40 nm) bottom electrodes with a Ti (7 nm) adhesion layer are deposited onto 1 cm^2 Si/SiO₂ (300 nm) substrates by DC magnetron sputtering. Next, the substrates are cleaned in an Ar plasma using reactive-ion-etching (with an RF power of 100 W and a flow rate of 20 sccm for 2 min). A stainless-steel shadow mask is then applied, with an open square area $\sim 0.8 \times 0.8 \text{ cm}$, leaving the edges of the $1 \times 1 \text{ cm}$ substrates accessible for electrical measurements, by allowing direct electrical access to the bottom Pt electrode layer. After this, the substrates are loaded into a FCVA chamber and pumped to a base pressure $\sim 5 \times 10^{-7} \text{ mbar}$. 15, 20 and 40 nm ta-C films are then deposited at room temperature. Different thicknesses are prepared by calibrating the deposition rate of the FCVA and adjusting the deposition time.

2.1. N_2 implantation

The samples are then N_2 implanted at ion doses of 3×10^{13} , 1×10^{14} , 3×10^{14} , 1×10^{15} and $3 \times 10^{15} \text{ cm}^{-2}$. In order to ensure

incorporation of N^+ ion species into the ta-C film, implantation energies are determined using the Stopping Range of Ions in Matter (SRIM) code [40]. The N^+ ion-energy defines the depth of penetration, or mean projected range R_p , into the sample, and the variance, ΔR_p , in the projected range is the straggle [40]. R_p and ΔR_p can be calculated using SRIM [40], and the values for our case are shown in Table 1. In order to determine the dose (flux) of ions that is needed to achieve the desired ion concentration within the film we use [40]:

$$n(R_p) = \frac{\phi}{\sqrt{2\pi} \Delta R_p} \cong \frac{0.4\phi}{\Delta R_p} \quad (1)$$

where $n(R_p)$ [cm^{-3}] is the peak ion concentration, which is defined by the dose, ϕ [cm^{-2}] and ΔR_p .

Previous studies [41,42] on N_2 implanted ta-C reported changes in the field-emission properties as well as electronic properties at N_2 implantation doses $\sim 10^{14} \text{ cm}^{-2}$, with implanted ion concentrations $< 1\%$. Thus, here we use N_2 doses from 1×10^{13} to $3 \times 10^{15} \text{ cm}^{-2}$. For 40, 20 and 15 nm films the implantation energies are 20, 10 and 6 keV, respectively. All implantations are carried out using a 200 kV Danfysik high-current ion-implanter with a beam current of 5 μA in a vacuum of $6.2 \times 10^{-6} \text{ mbar}$. Some samples are implanted over their entire area, while for others a mask comprising a Cu TEM grid (fixed onto the sample using Ag paint) is used to provide both implanted and reference unimplanted regions.

2.2. X-ray photoelectron spectroscopy

XPS measurements are performed using a Kratos Analytical AXIS Nova XPS spectrometer equipped with a monochromatic source (Al-K α ; 1486.6 eV). The core-level C1s spectra are collected from three different regions of each sample using a pass energy of 20 eV, an energy step of 0.15 eV, dwell time of 100 ms and a spot size of $\sim 300 \mu\text{m}$. The spectra are then fitted with mixed Gaussian-Lorentzian functions after performing standard XPS analysis processes, such as Shirley background subtraction [43], charge compensation [44] and internal spectrum calibration [45].

2.3. Raman spectroscopy

Unpolarised Raman spectra are recorded at 244, 325, 457, 514.5 and 633 nm using a Renishaw InVia spectrometer equipped with a Leica DM LM microscope. All spectra measured at 244 and 325 nm are corrected by subtracting the background signal due to the optics. This is done by measuring an Al mirror background signal and normalising this so that the atmospheric N_2 peak at 2332 cm^{-1} detected from the mirror measurement has the same intensity as the corresponding atmospheric N_2 peak detected on the sample [46]. The power on the sample is

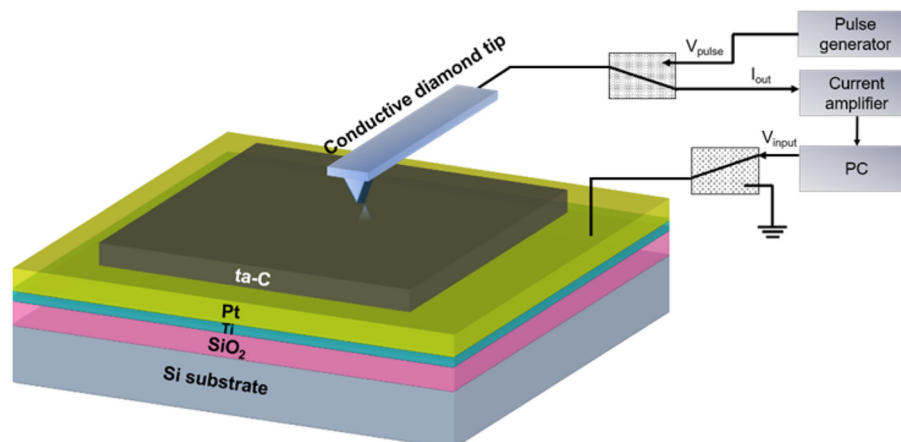


Fig. 1. Schematic CAFM set-up used for RS measurements of films deposited on a Pt bottom electrode, with a doped conductive diamond probe top electrode.

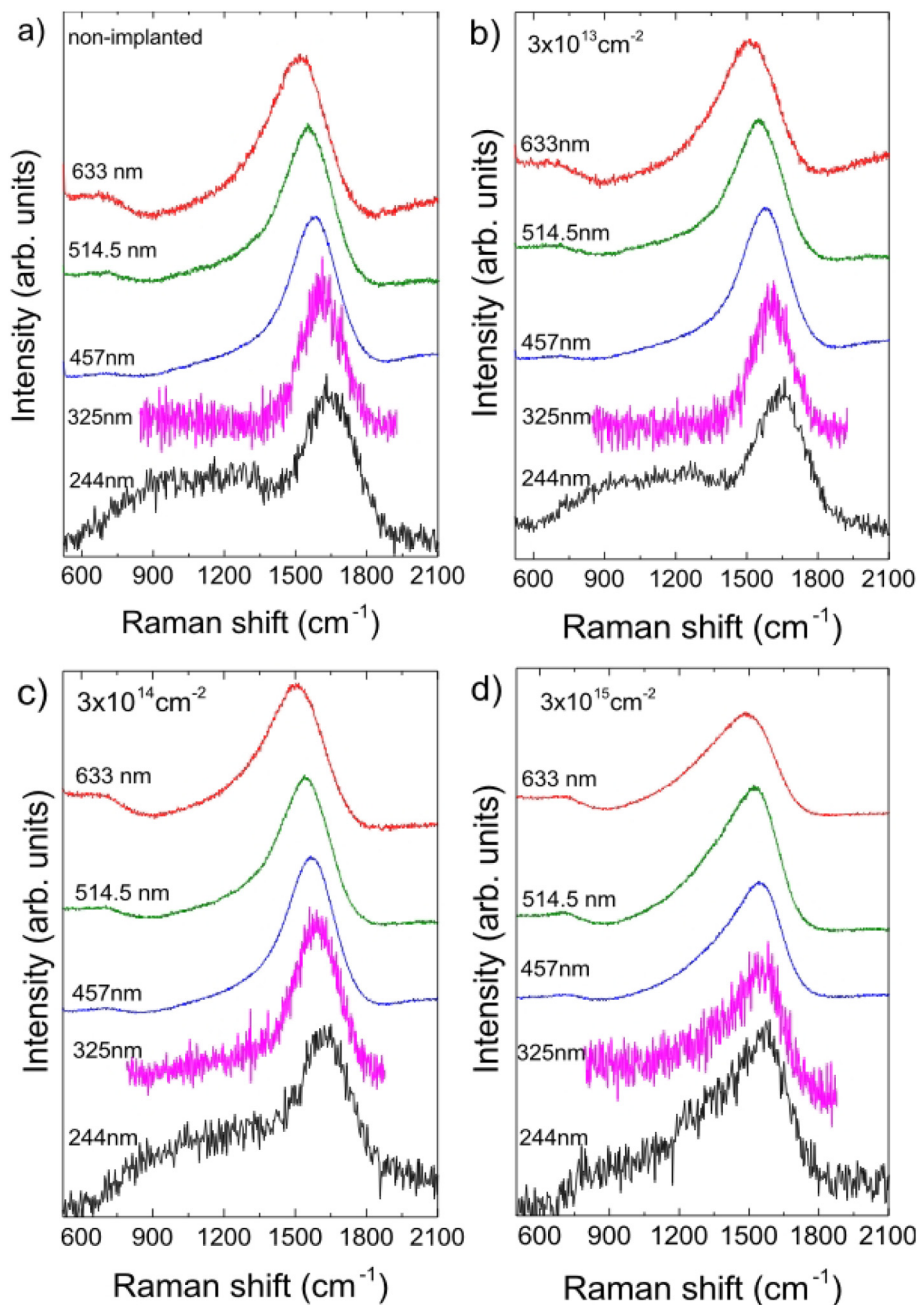


Fig. 2. Raman spectra of a 20 nm ta-C film (a) before and (b–d) after implantation at doses of (b) $3 \times 10^{13} \text{ cm}^{-2}$ (c) $3 \times 10^{14} \text{ cm}^{-2}$ and (d) $3 \times 10^{15} \text{ cm}^{-2}$.

$\sim 5 \mu\text{W}$ and the samples are placed on a spinning stage rotating at 3000 rpm. These procedures ensure that no visible damage occurs, and no change of peak shape during the Raman measurements. For visible wavelengths five spectra are taken per sample. The spectra are fitted using a Lorentzian for the D peak and Breit-Wigner-Fano (BWF) for the G peak [46].

2.4. Atomic force microscopy

The surface topography and local conductivity variations are analysed using a Veeco Innova scanning probe microscopy system (Bruker corp.) in CAFM mode, with conductive doped-diamond coated Si cantilevers (Bruker AFM probes, DDESP-FM-10). These tips have a nominal radius $\sim 100 \text{ nm}$, a resonant frequency $\sim 60\text{--}100 \text{ kHz}$ and a force constant $\sim 1\text{--}5 \text{ Nm}^{-1}$ [47]. They are ideal for RS measurements since, compared to conventional metal-coated CAFM

probes, they have a high current carrying capacity and good wear resistance (see e.g. Refs. [48, 49]). For RS measurements, the CAFM tip acts as a top electrode, directly contacting the ta-C films, while the Pt layer beneath the film acts as a bottom electrode and is electrically connected to the CAFM system to complete the circuit path. CAFM conductivity maps and I-V curves are acquired in contact mode by applying a potential to the Pt bottom electrode, with the tip grounded. Fig. 1 shows a schematic of the CAFM set-up. All measurements are performed at room temperature in an ambient air-atmosphere.

3. Results and discussions

We use Raman spectroscopy to extract the ta-C bonding parameters. All carbons show common features in their Raman spectra in the 800 to 2000 cm^{-1} region: the so called G and D peaks, at ~ 1560 and

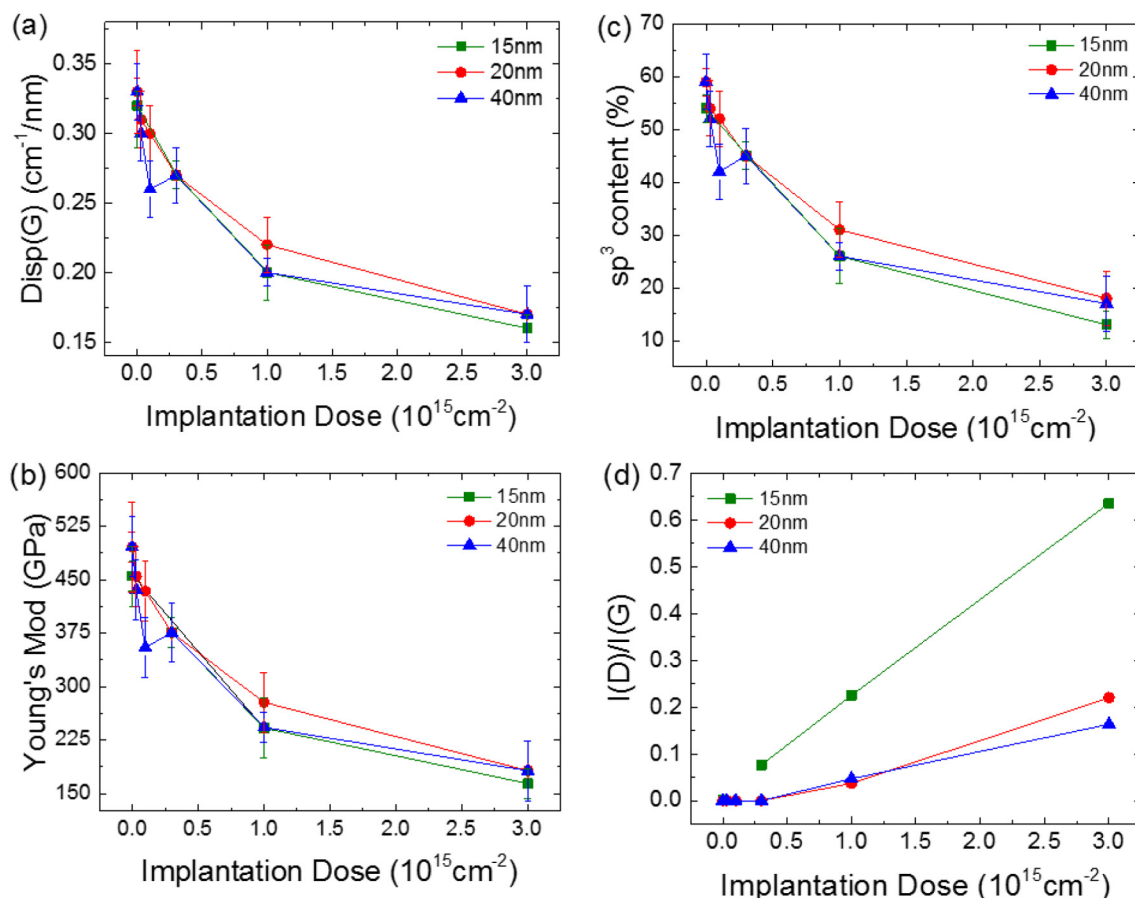


Fig. 3. (a) Disp(G), (b) Young's modulus and (c) sp^3 content from multi-wavelength Raman spectroscopy for 15, 20 and 40 nm samples as a function of dose; (d) I(D)/I(G) at 514.5 nm.

1360 cm^{-1} [50] and the T peak at $\sim 1060 \text{ cm}^{-1}$ which can be detected only for UV excitation [51,52]. The G peak is due to the bond stretching of all pairs of sp^2 atoms in both rings and chains [53]. The D peak is due to the breathing modes of sp^2 atoms in rings [53–55]. The T peak is assigned to the C-C sp^3 vibrations [56,57].

Ref. [53] proposed an empirical three-stage model to describe the Raman spectra of carbon films measured at any excitation energy. The evolution of the Raman spectra is understood by considering an amorphization trajectory, starting from graphite. The main factor affecting peaks' position, width and intensity is the clustering of the sp^2 phase. This can in principle vary independently from the sp^3 content, so that for a given sp^3 content and excitation energy, we can have a number of different Raman spectra, or, equivalently, similar Raman spectra for different sp^3 contents. For UV excitation, an increase in clustering always lowers the G peak position, Pos(G). However, in visible Raman the G peak does not depend monotonically on cluster size. If two samples have similar Pos(G) in visible Raman but different ones in UV Raman, the sample with the lower Pos(G) in the UV has higher sp^2 clustering [51,53]. A multi-wavelength Raman analysis is thus important to fully characterize the samples. A very useful parameter is then the G peak dispersion Disp(G) [51,53], i.e. the rate of change of Pos(G) with excitation wavelength. The G peak disperses in disordered carbons, where Disp(G) is proportional to the amount of disorder [51,58–60]. Pos(G) increases as the excitation wavelength decreases [51], thus Disp(G) increases with disorder [51,58–60]. Another useful parameter is the Full-Width-at-Half-Maximum of the G peak, FWHM(G). Both FWHM(G) and Disp(G) always increase as the disorder increases, at every excitation wavelength. Thus Disp(G) allows one to estimate the Young's modulus, density and sp^3 content, as explained in detail in previous works [51,58–60].

A multi-wavelength Raman characterisation is carried out before and after implantation. Representative spectra for a 20 nm sample before and after implantation with doses of 3×10^{13} , 3×10^{14} and $3 \times 10^{15} \text{ cm}^{-2}$ are shown in Fig. 2.

The extracted bonding parameters for all implantation doses for the 15, 20 and 40 nm ta-C films are shown in Fig. 3. Raman spectroscopy indicates a decrease in Young's modulus (Fig. 3b) and sp^3 content (Fig. 3c) as the implantation dose is increased. An increase in I(D)/I(G) with increasing implantation is also seen, Fig. 3d.

The spectra for unimplanted ta-C films and those implanted up to a $3 \times 10^{14} \text{ cm}^{-2}$ have a negligible D peak, with I(D)/I(G) < 0.1. This corresponds to a very small cluster size < 0.5 nm [37,38,61]. An increase in sp^2 cluster size is seen for higher implantation doses, as shown by the increasing I(D)/I(G) in Fig. 3d. The increase is most pronounced in the 15 nm film, where the cluster size is up to 1.1 nm at $3 \times 10^{15} \text{ cm}^{-2}$.

Turning now to the XPS analysis, core-level C1s spectra are acquired for all implanted and unimplanted films, with the results for the 20 and 40 nm thick samples in Fig. 4. Deconvolution with mixed Gaussian-Lorentzian functions reveals peaks at 284.4 and 285.5 eV, representing sp^2 and sp^3 bonding configurations respectively, while the weak shoulder peak at $\sim 286.5 \text{ eV}$ corresponds to carbon-oxygen bonding (C-O) [62–64].

After N_2 implantation, a change in bonding is observed, Fig. 4b,d, with a broadened C1s and reduced peak intensities. Analysis of the spectra reveals a decrease in sp^3 and an increase in sp^2 with increasing dose, as summarised in Fig. 5. For example, for the 40 nm film, XPS indicates that the unimplanted film has $\sim 65\% sp^3$, Fig. 5a. After N_2 implantation at $3 \times 10^{15} \text{ cm}^{-2}$, the sp^3 decreases to $\sim 23\%$, while the sp^2 increase to $\sim 65\%$, Fig. 5a. Similar effects are seen in the 20 nm implanted film, Fig. 5b, consistent with the Raman data of Fig. 3.

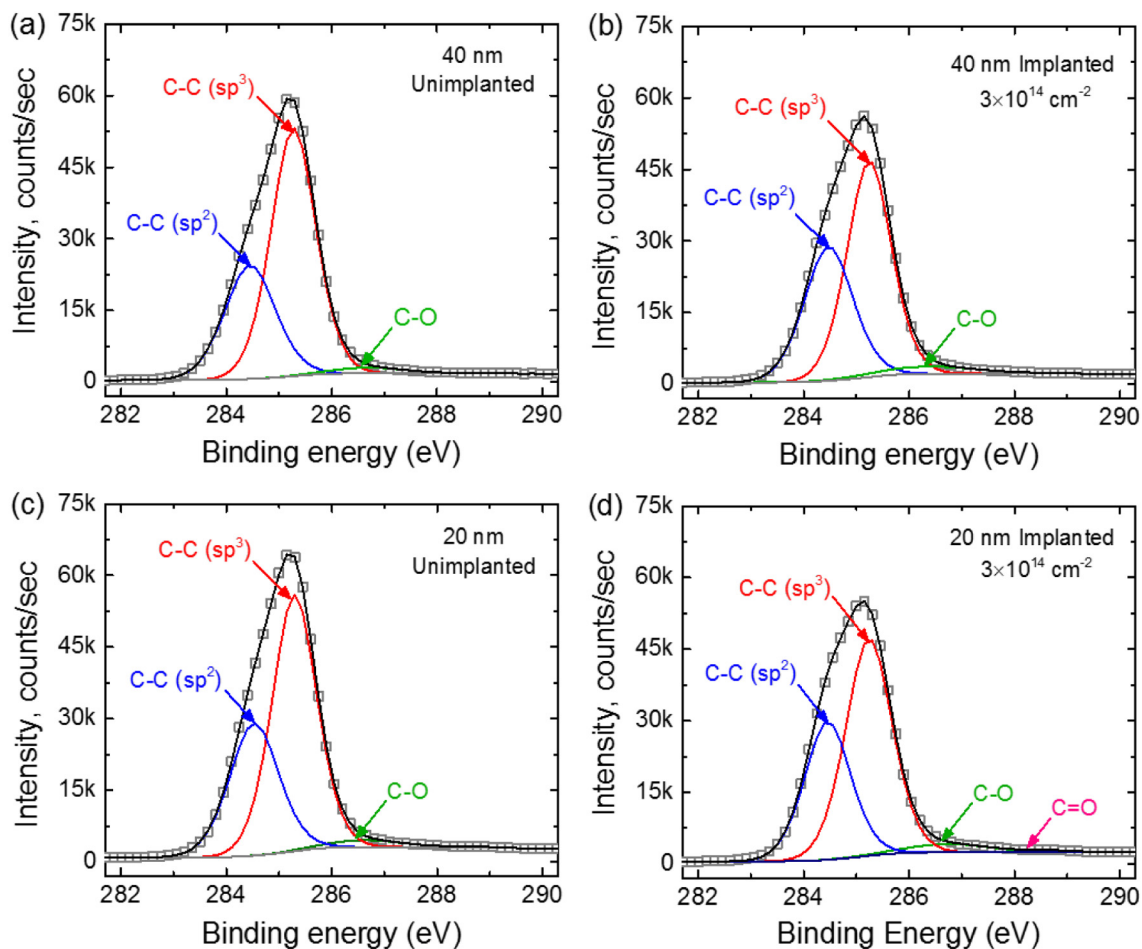


Fig. 4. High-resolution C1s XPS spectra of (a,b) 40 nm and (c,d) 20 nm films measured (a,c) before and (b,d) after implantation at $3 \times 10^{14} \text{ cm}^{-2}$.

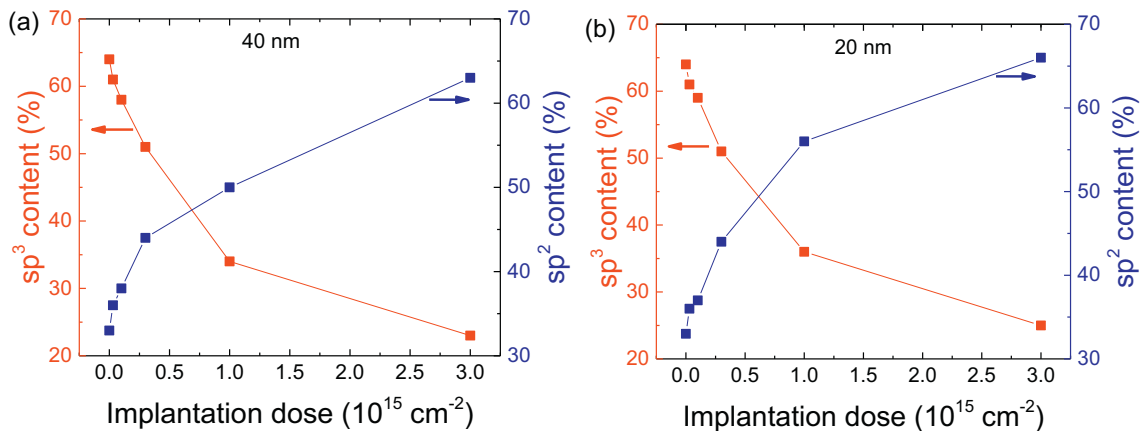


Fig. 5. Effect of N_2 implantation dose on the XPS-derived concentration of sp^3 and sp^2 bonds in (a) 40 nm and (b) 20 nm ta-C films.

Topographic (AFM) imaging shows that implantation does not significantly change the surface roughness. For example Fig. 6 shows a 20 nm film containing both unimplanted regions and regions implanted at $1 \times 10^{14} \text{ cm}^{-2}$. The average root-mean-square (RMS) roughness of the unimplanted film is $\sim 0.2 \text{ nm}$, consistent with that expected for FCVA ta-C films [65–67], whereas for the implanted areas the roughness is only slightly higher, at $\sim 0.22 \text{ nm}$. There is however a noticeable change in overall sample height (volume) across the implanted to unimplanted boundary, with the surface of the implanted region being higher, Fig. 6b. Such a change is consistent with implantation leading to a reduction in density due to an increasing sp^2 content upon implantation (for this sample

the initial and final (post-implantation) sp^3 content, as determined by Raman analysis, is $\sim 60\%$ and $\sim 55\%$ respectively). The implanted region is also more electrically conductive, as revealed by CAFM scans, Fig. 6c. Implanted regions are also visible via optical microscopy, with implanted areas showing an increase in optical absorption, Fig. 7.

To quantify the role of N_2 implantation on RS, we perform CAFM measurements. Current-voltage characteristics (I-V curves) are obtained by ramping up V and measuring the resultant tip current with the CAFM probe stationary. For example, Fig. 8a,b,c plot the I-V characteristics for 40, 20 and 15 nm films both unimplanted and implanted at a dose of $3 \times 10^{15} \text{ cm}^{-2}$. All curves exhibit unipolar RS, remaining in a HRS until

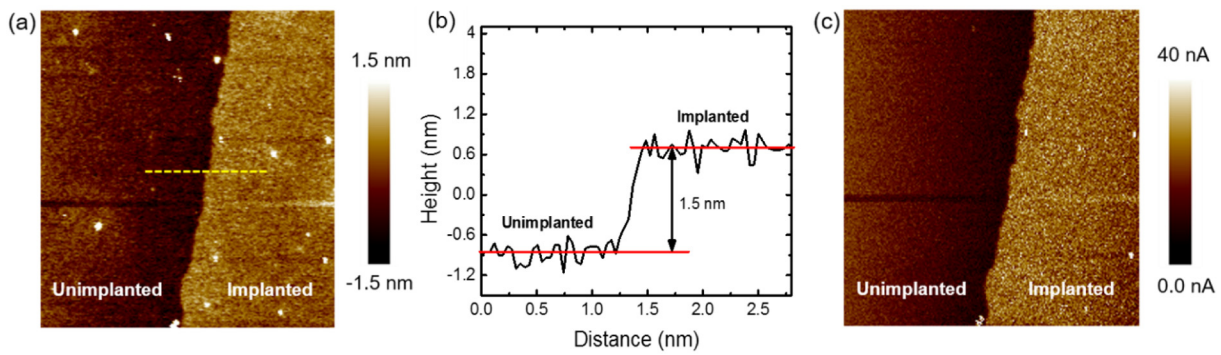


Fig. 6. AFM (a) topography image and (b) height profile across the boundary of implanted and unimplanted regions of a 20 nm film (dose $1 \times 10^{14} \text{ cm}^{-2}$). (c) CAFM conductivity scan over the same region (for 3.5 V, with the tip grounded). Both AFM scans are $8 \times 10 \mu\text{m}^2$ in size.

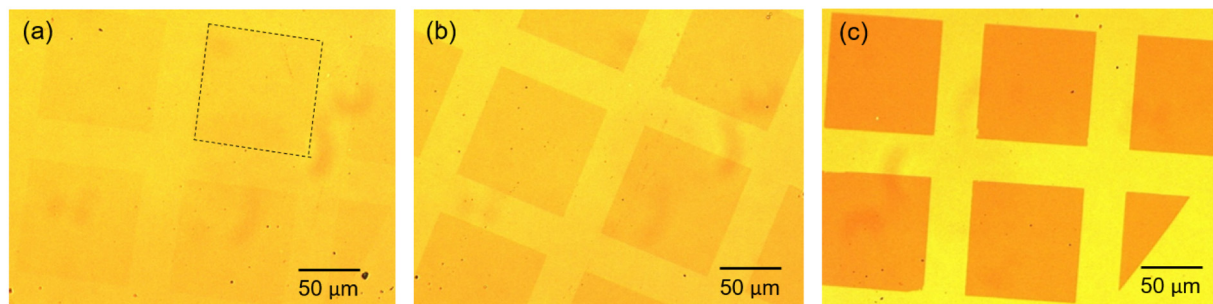


Fig. 7. Optical microscope images of 20 nm films containing both unimplanted and implanted regions for implantations doses of (a) $3 \times 10^{13} \text{ cm}^{-2}$, (b) $1 \times 10^{14} \text{ cm}^{-2}$ and (c) $3 \times 10^{14} \text{ cm}^{-2}$. Implanted regions show a darker contrast due to increased optical absorption.

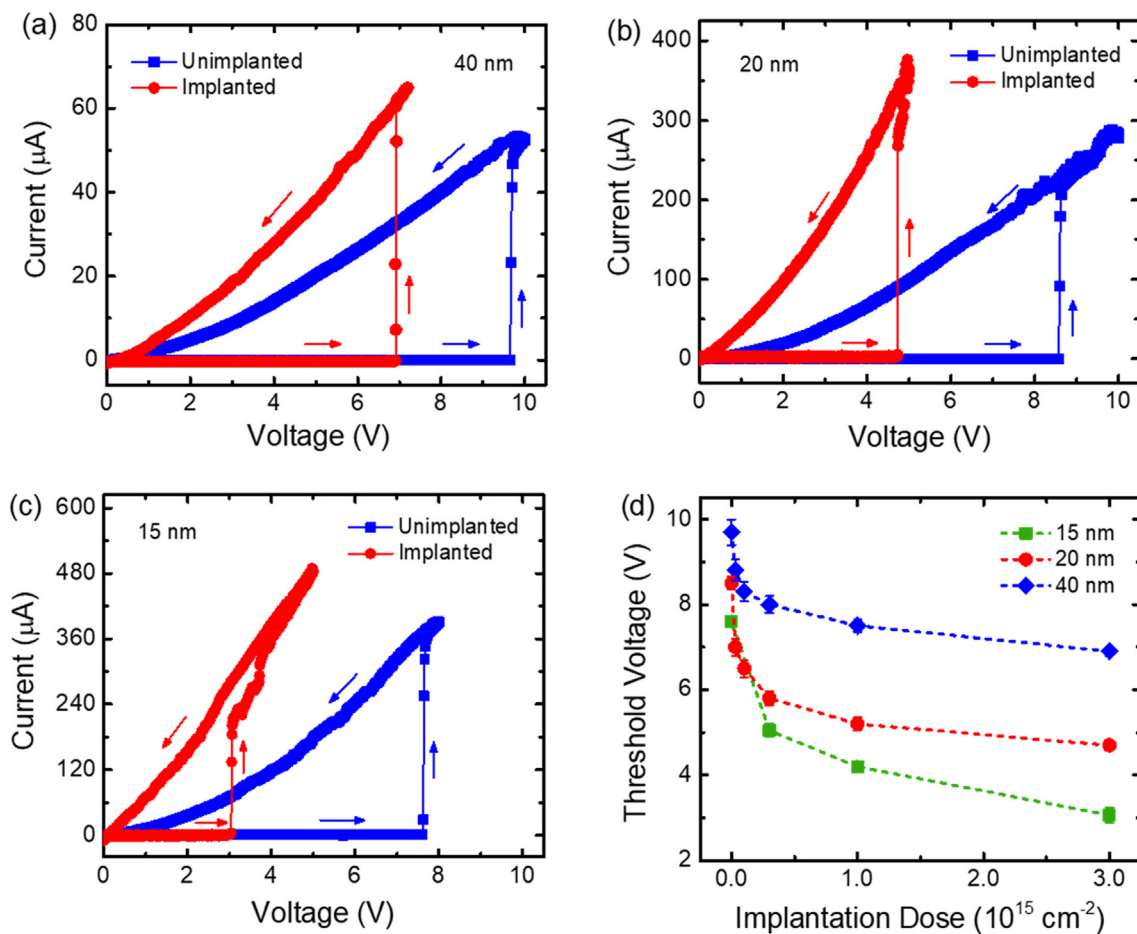


Fig. 8. CAFM I-V responses for unimplanted (blue lines/squares) and N_2 -implanted (red lines/circles) ta-C films with thickness (a) 40 nm, (b) 20 nm, (c) 15 nm, implanted a $3 \times 10^{15} \text{ cm}^{-2}$; (d) variation of V_{th} as a function of implantation dose for a given film thickness.

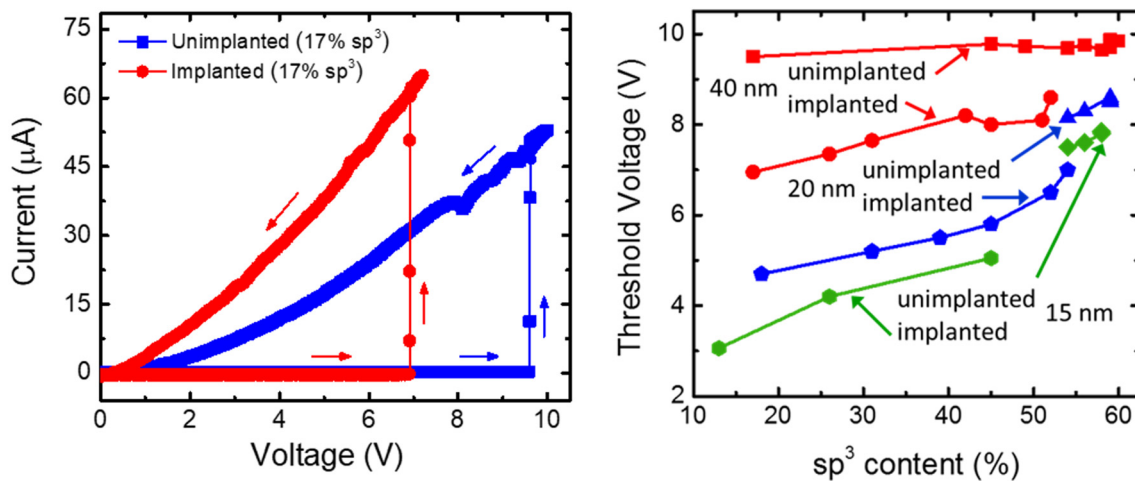


Fig. 9. (a) I–V curves for an unimplanted film with $\sim 17\%$ sp^3 (blue line/squares) and an implanted sample with a post-implantation $sp^3 \sim 17\%$ (red line/circles). Both samples are 40 nm thick and the implantation dose $\sim 3 \times 10^{15} \text{ cm}^{-2}$. (b) Threshold switching voltage, V_{th} , as a function of sp^3 content for all (unimplanted and implanted) films examined in this study.

a characteristic threshold switching voltage (V_{th}) is reached, at which point they switch suddenly to a LRS, a behaviour characteristic of sp^3 -rich amorphous carbon films [23,24,26–28].

From Fig. 8 it can be seen that V_{th} is ~ 9.7 , 8.5 and 7.6 V for the 40, 20 and 15 nm unimplanted films, high values which reflect both the highly resistive nature of the as-deposited ta-C films and a high tip-sample contact resistance. After N_2 implantation, V_{th} for all samples is significantly reduced, with the reduction for the thinnest ta-C being the most marked, from ~ 7.6 to ~ 3 V. The effects of N_2 implantation dose on the threshold switching voltage for all film thicknesses and implantation doses used are summarised in Fig. 8d.

Fig. 8 shows that that nitrogen implantation makes the switching of ta-C films from HRS to LRS (i.e. SET switching) easier, by reducing V_{th} . We assign this to changes in the size and distribution of sp^2 clusters as a result of implantation. Indeed, the average sp^2 cluster size extracted from our Raman measurements increases, as shown in Fig. 3d. Molecular dynamics simulations [28,68] indicate that SET switching in ta-C films is likely caused by an electrically-driven (Joule heating) re-hybridization of sp^3 -bonded atoms to a sp^2 bonding configuration (with the total change in sp^3 content below 2%, [28]), resulting in the formation of a conducting pathway between the device electrodes.

The electrically-driven formation of sp^2 -hybridized conducting filaments in a predominantly sp^3 -rich ta-C matrix is facilitated by ion implantation, since this introduces sp^2 clusters in regions lying along the ions' trail [69], which, in turn, produce a pre-switching sp^2 cluster distribution particularly susceptible to SET switching. The notion that it is the implantation process per se and its resulting effects on the distribution of sp^2 clusters that facilitates SET switching, rather than simply the film's initial sp^3/sp^2 content, is substantiated by I–V measurement on a low ($\sim 17\%$) sp^3 content film, Fig. 9a. The implanted film has a significantly lower V_{th} , in spite of having almost the same sp^3 content. Fig. 9b plots V_{th} as a function of sp^3 content for all films. This shows that in all cases V_{th} is significantly lower for implanted films.

Thus, the RS behaviour, in terms of V_{th} , of ta-C films can be controlled and tailored by varying the N_2 implantation dose.

4. Conclusions

We studied the structural and electrical characteristics of N_2 -implanted and unimplanted ta-C films for non-volatile resistive-switching memory applications. Both Raman and XPS measurements indicate changes in sp^3 and sp^2 bonding after implantation, correlated with the

implantation dose. An increase in sp^2 cluster size with increasing implantation dose is also observed. Both unimplanted and implanted films show unipolar resistive-switching, with a characteristic threshold voltage required to switch the films from the high-resistance to the low-resistance state. The switching voltages are significantly reduced upon implantation, up to $\sim 60\%$. We attribute this to implantation-induced increase in the size and number of sp^2 clusters, along with changes in their (spatial and size) distribution, thus highlighting the importance of sp^2 clustering in resistive-switching of ta-C films.

Acknowledgements

We acknowledge funding from EU FP7 project CareRAMM, FP7/2007-2013, grant agreement n^o 309980 and EPSRC grants EP/K017160/1 and EP/M002438/1. Nitrogen implantation was carried out at the Surrey Ion Beam Centre, University of Surrey, UK. XPS measurements were done at the National EPSRC XPS User's Service (NEXUS) at Newcastle University, UK, an EPSRC Mid-Range Facility.

References

- [1] D.S. Jeong, R. Thomas, R.S. Katiyar, J.F. Scott, H. Kohlstedt, A. Petraru, C.S. Wang, Emerging memories: resistive switching mechanisms and current status, Rep. Prog. Phys. 75 (2012) 076502, <http://dx.doi.org/10.1088/0034-4885/75/7/076502>.
- [2] R. Waser, R. Dittmann, G. Staikov, K. Szot, Redox-based resistive switching memories – nanoionic mechanisms, prospects, and challenges, Adv. Mater. 21 (2009) 2632–2663, <http://dx.doi.org/10.1002/adma.200900375>.
- [3] F. Hui, E. Gustan-Gutierrez, S. Long, Q. Liu, A.K. Ott, A.C. Ferrari, M. Lanza, Graphene and related materials for resistive random access memories, Adv. Electr. Mater. 3 (2017) 1600195, <http://dx.doi.org/10.1002/aelm.201600195>.
- [4] H.S.P. Wong, S. Salahuddin, Memory leads the way to better computing, Nat. Nanotechnol. 10 (2015) 191–194, <http://dx.doi.org/10.1038/nnano.2015.29>.
- [5] S. Kim, C. Du, P. Sheridan, W. Ma, S. Choi, W.D. Lu, Experimental demonstration of a second-order memristor and its ability to biorealistically implement synaptic plasticity, Nano Lett. 15 (2015) 2203–2211, <http://dx.doi.org/10.1021/acs.nanolett.5b00697>.
- [6] C.D. Wright, P. Hosseini, J.A.V. Diodado, Beyond von-Neumann computing with nanoscale phase-change memory devices, Adv. Funct. Mater. 23 (2013) 2248–2254, <http://dx.doi.org/10.1002/adfm.201202383>.
- [7] S. Raoux, M. Wuttig, Phase Change Materials, Springer, Boston, MA, 2008.
- [8] A. Sawa, Resistive switching in transition metal oxides, Mater. Today 11 (2008) 28–36, [http://dx.doi.org/10.1016/S1369-7021\(08\)70119-6](http://dx.doi.org/10.1016/S1369-7021(08)70119-6).
- [9] B.J. Choi, D.S. Jeong, S.K. Kim, C. Rohde, S. Choi, J.H. Oh, H.J. Kim, C.S. Wang, K. Szot, R. Waser, B. Reichenberg, S. Tiedke, Resistive switching mechanism of TiO₂ thin films grown by atomic-layer deposition, J. Appl. Phys. 98 (2005) 033715, <http://dx.doi.org/10.1063/1.2001146>.
- [10] Y. Watanabe, J.G. Bednorz, A. Bietsch, C. Gerber, D. Widmer, A. Beck, S.J. Wind, Current-driven insulator-conductor transition and nonvolatile memory in chromium-doped SrTiO₃ single crystals, Appl. Phys. Lett. 78 (2001) 3738–3740, <http://dx.doi.org/10.1063/1.1377617>.
- [11] A.N. Chen, S. Haddad, Yi-Ching Wu, Tzu-Ning Fang, Zhida Lan, S. Avanzino,

- S. Pangrle, M. Buynoski, M. Rathor, W. Cai, N. Tripsas, C. Bill, M. VanBuskirk, M. Taguchi, Non-volatile resistive switching for advanced memory applications, IEEE International Electron Devices Meeting, 2005, IEDM Technical Digest, IEEE, 2005, pp. 746–749, <http://dx.doi.org/10.1109/IEDM.2005.1609461>.
- [12] I.G. Baek, M.S. Lee, S. Seo, M.J. Lee, D.H. Seo, D.S. Suh, J.C. Park, S.O. Park, H.S. Kim, I.K. Yoo, U-In Chung, J.T. Moon, Highly scalable non-volatile resistive memory using simple binary oxide driven by asymmetric bipolar voltage pulses, in: IEDM Technical Digest, IEEE International Electron Devices Meeting, 2004, IEEE, 2004, pp. 587–590, <http://dx.doi.org/10.1109/IEDM.2004.1419228>.
- [13] A. Prakash, D. Jana, S. Maikap, TaO(x)-based resistive switching memories: prospective and challenges, *Nanoscale Res. Lett.* 8 (2013), <http://dx.doi.org/10.1186/1556-276X-8-418>.
- [14] J. Kim, C. Ko, A. Frenzel, S. Ramanathan, J.E. Hoffman, Nanoscale imaging and control of resistance switching in VO₂ at room temperature, *Appl. Phys. Lett.* 96 (2010) 213106, <http://dx.doi.org/10.1063/1.3435466>.
- [15] C. Walczyk, C. Wenger, R. Sohal, M. Lukosius, A. Fox, J. Dąbrowski, D. Wolansky, B. Tillack, H.-J. Müssig, T. Schroeder, Pulse-induced low-power resistive switching in HfO₂ metal-insulator-metal diodes for nonvolatile memory applications, *J. Appl. Phys.* 105 (2009) 114103, <http://dx.doi.org/10.1063/1.3139282>.
- [16] S.Q. Liu, N.J. Wu, A. Ignatiev, Electric-pulse-induced reversible resistance change effect in magnetoresistive films, *Appl. Phys. Lett.* 76 (2000) 2749–2751, <http://dx.doi.org/10.1063/1.126464>.
- [17] A. Beck, J.G. Bednorz, C. Gerber, C. Rossel, D. Widmer, Reproducible switching effect in thin oxide films for memory applications, *Appl. Phys. Lett.* 77 (2000) 139–141, <http://dx.doi.org/10.1063/1.1269902>.
- [18] S. Yoo, T. Eom, T. Gwon, C.S. Hwang, Bipolar resistive switching behavior of an amorphous Ge₂Sb₂Te₅ thin films with a Te layer, *Nano* 7 (2015) 6340–6347, <http://dx.doi.org/10.1039/c5nr01361e>.
- [19] H.Y. Jeong, J.Y. Kim, J.W. Kim, J.O. Hwang, J.-E. Kim, J.Y. Lee, T.H. Yoon, B.J. Cho, S.O. Kim, R.S. Ruoff, S.-Y. Choi, Graphene oxide thin films for flexible nonvolatile memory applications, *Nano Lett.* 10 (2010) 4381–4386, <http://dx.doi.org/10.1021/nl101902k>.
- [20] Z. Yin, Z. Zeng, J. Liu, Q. He, P. Chen, H. Zhang, Memory devices using a mixture of MoS₂ and graphene oxide as the active layer, *Small* 9 (2013) 727–731, <http://dx.doi.org/10.1002/sml.201201940>.
- [21] V.K. Nagareddy, M.D. Barnes, F. Zipoli, K.T. Lai, A.M. Alexeev, M.F. Gracian, C.D. Wright, Multilevel ultrafast flexible nanoscale nonvolatile hybrid graphene oxide–titanium oxide memories, *ACS Nano* 11 (2017) 3010–3021, <http://dx.doi.org/10.1021/acsnano.6b08668>.
- [22] A. Sebastian, A. Pauza, C. Rossel, R.M. Shelby, Resistance switching at the nanometre scale in amorphous carbon, *New J. Phys.* 13 (2011) 013020, <http://dx.doi.org/10.1088/1367-2630/13/1/013020>.
- [23] F. Kreupl, R. Bruchhaus, P. Majewski, J.B. Philipp, R. Symanczyk, T. Happ, C. Arndt, M. Vogt, R. Zimmermann, A. Buerke, A.P. Graham, M. Kund, Carbon-based resistive memory, 2008 IEEE International Electron Devices Meeting (IEDM), IEEE, 2008, pp. 1–4, <http://dx.doi.org/10.1109/IEDM.2008.4796740>.
- [24] D. Fu, D. Xie, T. Feng, C. Zhang, J. Niu, H. Qian, L. Liu, Unipolar resistive switching properties of diamondlike carbon-based RRAM devices, *IEEE Electron Device Lett.* 32 (2011) 803–805, <http://dx.doi.org/10.1109/LED.2011.2132750>.
- [25] Y. Chai, Y. Wu, K. Takei, H.-Y. Chen, S. Yu, P.C.H. Chan, A. Javey, H.-S.P. Wong, Nanoscale bipolar and complementary resistive switching memory based on amorphous carbon, *IEEE Trans. Electron Devices* 58 (2011) 3933–3939, <http://dx.doi.org/10.1109/TED.2011.2164615>.
- [26] J. Xu, D. Xie, T. Feng, C. Zhang, X. Zhang, P. Peng, D. Fu, H. Qian, T.-L. Ren, L. Liu, Scaling-down characteristics of nanoscale diamond-like carbon based resistive switching memories, *Carbon* 75 (2014) 255–261, <http://dx.doi.org/10.1016/j.carbon.2014.03.061>.
- [27] J. Xu, D. Xie, C. Zhang, X. Zhang, P. Peng, H. Qian Di Fu, T.-L. Ren, L. Liu, Pulse widths dependence of programming and erasing behaviors for diamond like carbon based resistive switching memories, *Appl. Phys. Lett.* 105 (2014) 172101, <http://dx.doi.org/10.1063/1.4898345>.
- [28] W.W. Koelmans, T. Bachmann, F. Zipoli, A.K. Ott, C. Dou, A.C. Ferrari, O. Cojocar-Mirédin, S. Zhang, C. Scheu, M. Wuttig, V.K. Nagareddy, M.F. Gracian, A.M. Alexeev, C.D. Wright, V.P. Jonnalagadda, A. Curioni, A. Sebastian, E. Eleftheriou, Carbon-based resistive memories, IEEE International Memory Workshop (IMW), 2016 IEEE, 2016, pp. 1–4, <http://dx.doi.org/10.1109/IMW.2016.7493569>.
- [29] F. Zhuge, W. Dai, C.L. He, A.Y. Wang, Y.W. Liu, M. Li, Y.H. Wu, P. Cui, R.-W. Li, Nonvolatile resistive switching memory based on amorphous carbon, *Appl. Phys. Lett.* 96 (2010) 163505, <http://dx.doi.org/10.1063/1.3406121>.
- [30] B. Ren, L. Wang, L. Wang, J. Huang, K. Tang, Y. Lou, D. Yuan, Z. Pan, Y. Xia, Investigation of resistive switching in graphite-like carbon thin film for non-volatile memory applications, *Vacuum* 107 (2014) 1–5, <http://dx.doi.org/10.1016/j.vacuum.2014.03.021>.
- [31] P. Peng, D. Xie, Y. Yang, C. Zhou, S. Ma, T. Feng, H. Tian, T. Ren, Bipolar and unipolar resistive switching effects in Al/DLC/W structure, *J. Phys. D: Appl. Phys.* 45, 365103. doi:10.1088/0022-3727/45/42/429501.
- [32] F. Kreupl, Carbon Memory Assessment, <https://arxiv.org/abs/1408.4600>, (2014).
- [33] <http://www.lenntech.com/periodic/elements/c.htm>.
- [34] S. Qin, J. Zhang, D. Fu, D. Xie, Y. Wang, H. Qian, L. Lu, Z. Yu, A physics/circuit-based switching model for carbon-based resistive memory with sp²/sp³ cluster conversion, *Nano* 4 (2012) 6658–6663, <http://dx.doi.org/10.1039/c2nr31180a>.
- [35] S. Grigull, W. Jacob, D. Henke, C. Spaeth, L. Stümmchen, W. Sigle, Transport and structural modification during nitrogen implantation of hard amorphous carbon films, *J. Appl. Phys.* 83 (1998) 5185–5194, <http://dx.doi.org/10.1063/1.367338>.
- [36] B. Kleinsorge, A.C. Ferrari, J. Robertson, W.I. Milne, Influence of nitrogen and temperature on the deposition of tetrahedrally bonded amorphous carbon, *J. Appl. Phys.* 88 (2000) 1149–1157, <http://dx.doi.org/10.1063/1.373790>.
- [37] S. Rodil, W.I. Milne, J. Robertson, L. Brown, Maximized sp³ bonding in carbon nitride phases, *Appl. Phys. Lett.* 77 (2000) 1458 <https://doi.org/10.1063/1.1308273>.
- [38] A.C. Ferrari, S.E. Rodil, J. Robertson, Interpretation of infrared and Raman spectra of amorphous carbon nitrides, *Phys. Rev. B* 67 (2003) 155306, <http://dx.doi.org/10.1103/PhysRevB.67.155306>.
- [39] M.C. Polo, J.L. Andujar, A. Hart, J. Robertson, W.I. Milne, Preparation of tetrahedral amorphous carbon films by filtered cathodic vacuum arc deposition, *Diam. Relat. Mater.* 9 (2000) 663–667, [http://dx.doi.org/10.1016/S0925-9635\(99\)00339-8](http://dx.doi.org/10.1016/S0925-9635(99)00339-8).
- [40] Ziegler, Biersack, SRIM.com.
- [41] Y.C. Chen, X.Y. Zhon, B. Kabius, J.M. Hiller, N.H. Tai, I.N. Lin, Improvement of field emission performance on nitrogen ion implanted ultrananocrystalline diamond films through visualization of structure modifications, *Diam. Relat. Mater.* 20 (2011) 238–241, <http://dx.doi.org/10.1016/j.diamond.2010.12.017>.
- [42] E.G. Gerstner, D.R. McKenzie, Fabrication and characterization of novel electronic devices using tetrahedral amorphous carbon, *Diam. Relat. Mater.* 7 (1998) 1172–1177, [http://dx.doi.org/10.1016/S0925-9635\(98\)00176-9](http://dx.doi.org/10.1016/S0925-9635(98)00176-9).
- [43] D.A. Shirley, High-resolution X-ray photoemission spectrum of the valence bands of gold, *Phys. Rev. B* 5 (1972) 4709–4714, <http://dx.doi.org/10.1103/PhysRevB.5.4709>.
- [44] J.B. Metson, Charge compensation and binding energy referencing in XPS analysis, *Surf. Interface Anal.* 27 (1999) 1069–1072, [http://dx.doi.org/10.1002/\(SICI\)1096-9918\(199912\)27:12<1069::AID-SIA677>3.3.CO;2-1](http://dx.doi.org/10.1002/(SICI)1096-9918(199912)27:12<1069::AID-SIA677>3.3.CO;2-1).
- [45] D. Dobler, S. Oswald, K. Wetzig, Calibration of XPS - energy scale for determination of the oxidation states of doping elements in SnO₂ powders, *Anal. Bioanal. Chem.* 374 (2002) 646–649, <http://dx.doi.org/10.1007/s00216-002-1448-y>.
- [46] C. Casiraghi, A.C. Ferrari, J. Robertson, Raman spectroscopy of hydrogenated amorphous carbons, *Phys. Rev. B* 72 (2005) 085401, <http://dx.doi.org/10.1103/PhysRevB.72.085401>.
- [47] Bruker AFM Probes, <http://www.BrukerAFMProbes.com/Ddesp-Aspx> (n.d.), <http://www.brukerafmprobes.com/p-3249-ddesp-10.aspx> (accessed February 28, 2017).
- [48] C. Kranz, Diamond as advanced material for scanning probe microscopy tips, *Electroanalysis* 28 (2016) 35–45, <http://dx.doi.org/10.1002/elan.201500630>.
- [49] H. Bhaskaran, B. Gotsmann, A. Sebastian, U. Drechsler, M.A. Lantz, M. Despont, P. Jaroenapiba, R.W. Carpick, Y. Chen, K. Sridharan, Ultralow nanoscale wear through atom-by-atom attrition in silicon-containing diamond-like carbon, *Nat. Nanotechnol.* 5 (2010) 181–185, <http://dx.doi.org/10.1038/nnano.2010.3>.
- [50] A.C. Ferrari, D.M. Basko, Raman spectroscopy as a versatile tool for studying the properties of graphene, *Nat. Nanotechnol.* 8 (2013) 235–246, <http://dx.doi.org/10.1038/nnano.2013.46>.
- [51] A.C. Ferrari, J. Robertson, Raman spectroscopy of amorphous, nanostructured, diamond-like carbon, and nanodiamond, *Philos. Trans. R. Soc. London, Ser. A* 362 (2004) 2477–2512, <http://dx.doi.org/10.1098/rsta.2004.1452>.
- [52] A.C. Ferrari, Determination of bonding in diamond-like carbon by Raman spectroscopy, *Diam. Relat. Mater.* 11 (2002) 1053–1061, [http://dx.doi.org/10.1016/S0925-9635\(01\)00730-0](http://dx.doi.org/10.1016/S0925-9635(01)00730-0).
- [53] A.C. Ferrari, J. Robertson, Interpretation of Raman spectra of disordered and amorphous carbon, *Phys. Rev. B* 61 (2000) 14095–14107, <http://dx.doi.org/10.1103/PhysRevB.61.14095>.
- [54] F. Tuinstra, J.L. Koenig, Raman spectrum of graphite, *J. Chem. Phys.* 53 (2003) 1126–1130 doi:10.1063/1.1674108.
- [55] C. Thomsen, S. Reich, Double resonant Raman scattering in graphite, *Phys. Rev. Lett.* 85 (2000) 5214–5217, <http://dx.doi.org/10.1103/PhysRevLett.85.5214>.
- [56] A.C. Ferrari, J. Robertson, Resonant Raman spectroscopy of disordered, amorphous, and diamond like carbon, *Phys. Rev. B* 64 (2001) 075414, <http://dx.doi.org/10.1103/PhysRevB.64.075414>.
- [57] S. Piscanec, F. Mauri, A.C. Ferrari, M. Lazzeri, J. Robertson, Ab initio resonant Raman spectra of diamond-like carbons, *Diam. Relat. Mater.* 14 (2005) 1078–1083, <http://dx.doi.org/10.1016/j.diamond.2004.11.043>.
- [58] A.C. Ferrari, Diamond-like carbon for magnetic storage disks, *Surf. Coat. Technol.* 180–181 (2004) 190–206.
- [59] C. Casiraghi, A.C. Ferrari, J. Robertson, R. Ohr, M.V. Gradoswki, D. Schneider, H. Hilgers, Ultra-thin carbon layer for high density magnetic devices, *Diam. Relat. Mater.* 13 (2004) 1480–1485, <http://dx.doi.org/10.1016/j.diamond.2003.12.018>.
- [60] A.C. Ferrari, A. Libassi, B.K. Tanner, V. Stolojan, J. Yuan, L.M. Brown, et al., Density, sp³ fraction, and cross-sectional structure of amorphous carbon films determined by x-ray reflectivity and electron energy-loss spectroscopy, *Phys. Rev. B* 62 (2000) 11089–11103, <http://dx.doi.org/10.1103/PhysRevB.62.11089>.
- [61] L.G. Cancado, A. Jorio, E.H. Martins Ferreira, F. Stavale, C.A. Achete, R.B. Capaz, M.V.O. Moutinho, A. Lombardo, T.S. Kulmala, A.C. Ferrari, Quantifying defects in graphene via Raman spectroscopy at different excitation energies, *Nano Lett.* 11 (2011) 3190–3196, <http://dx.doi.org/10.1021/nl201432g>.
- [62] A. Thompson, D.T. Attwood, E. Gullikson, M. Howells, X-ray Data Booklet (2009), URL, 2009. <http://xdb.lbl.gov>.
- [63] S. Jackson, Determining hybridization differences for amorphous carbon from the

- XPS C 1s envelope, Appl. Surf. Sci. 90 (1995) 195–203, [http://dx.doi.org/10.1016/0169-4332\(95\)00079-8](http://dx.doi.org/10.1016/0169-4332(95)00079-8).
- [64] P. Merel, M. Tabbal, M. Chaker, S. Moisa, J. Margot, Direct evaluation of the sp³ content in diamond-like-carbon films by XPS, Appl. Surf. Sci. 136 (1998) 105–110, [http://dx.doi.org/10.1016/S0169-4332\(98\)00319-5](http://dx.doi.org/10.1016/S0169-4332(98)00319-5).
- [65] C. Casiraghi, A.C. Ferrari, R. Ohr, A.J. Flewitt, D.C. Chu, J. Robertson, Dynamic roughening of tetrahedral amorphous carbon, Phys. Rev. Lett. 91 (2003) 226104-1 <https://doi.org/10.1103/PhysRevLett.91.226104>.
- [66] C. Casiraghi, A.C. Ferrari, J. Robertson, The smoothness of tetrahedral amorphous carbon, Diam. Relat. Mater. 14 (2005) 913–920, <http://dx.doi.org/10.1016/j.diamond.2005.01.023>.
- [67] M. Moseler, P. Gumbsch, C. Casiraghi, A.C. Ferrari, J. Robertson, The ultra-smoothness of diamond-like carbon surfaces, Science 309 (2005) 1545–1548, <http://dx.doi.org/10.1126/science.1114577>.
- [68] Y. He, J. Zhang, X. Guan, L. Zhao, Y. Wang, H. Qian, Z. Yu, Molecular dynamics study of the switching mechanism of carbon-based resistive memory, IEEE Trans. Electron Devices 57 (2010) 3434–3441, <http://dx.doi.org/10.1109/TED.2010.2076375>.
- [69] R.U.A. Khan, J.D. Carey, S.R.P. Silva, B.J. Jones, R.C. Barklie, Electron delocalization in amorphous carbon by ion implantation, Phys. Rev. B 63 (2001) 121201(R), <http://dx.doi.org/10.1103/PhysRevB.63.121201>.